

www.acsami.org Research Article

# Specific Ion Effects in Lanthanide—Amphiphile Structures at the Air—Water Interface and Their Implications for Selective Separation

Sangjun Yoo, Baofu Qiao, Travis Douglas, Wei Bu, Monica Olvera de la Cruz, and Pulak Dutta\*



Cite This: ACS Appl. Mater. Interfaces 2022, 14, 7504-7512



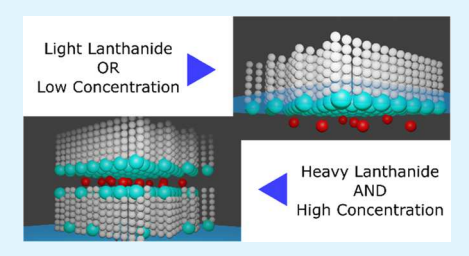
**ACCESS** I

Metrics & More

Article Recommendations

s) Supporting Information

**ABSTRACT:** The use of surfactants to attract dissolved ions to water surfaces and interfaces is an essential step in both solvent-based and solvent-free separation processes. We have studied the interactions of lanthanide ions in the aqueous subphase with monolayers of dihexadecyl phosphate at air—water interfaces. With heavier lanthanides (atomic number  $Z \geq 65$ ) in the subphase, the floating layer can be compressed to an area/molecule of about half the molecular cross section, indicating bilayer formation. X-ray fluorescence and reflectivity data support this conclusion. In the presence of lighter lanthanides (Z < 65), only monolayers are observed. Subphase-concentration-dependent studies using  $Er^{3+}$  (heavier) and  $Nd^{3+}$  (lighter) lanthanides



show a stepwise progression, with ions attaching to the monolayer only when the solution concentration is  $>3 \times 10^{-7}$  M. Above  $\sim 10^{-5}$  M, bilayers form but only in the presence of the heavier lanthanide. Grazing incidence X-ray diffraction shows evidence of lateral ion—ion correlations in the bilayer structure but not in monolayers. Explicit solvent all-atom molecular dynamics simulations confirm the elevated ion—ion correlation in the bilayer system. This bilayer structure isolates heavier lanthanides but not lighter lanthanides from an aqueous solution and is therefore a potential mechanism for the selective separation of heavier lanthanides.

KEYWORDS: specific ion effects, lanthanides, surfactant structure, air—water interface, synchrotron X-rays, X-ray reflectivity, Langmuir trough, solvent extraction

#### INTRODUCTION

The extraction and separation of lanthanide elements are commercially important because they are used to manufacture key components such as permanent magnets, batteries, and high-energy-density capacitors. Solvent extraction, 1,2 a process by which ions are transferred from aqueous solutions to organic liquid phases with the help of surfactants at the interface, is widely used to extract lanthanide ions dissolved in water (after lanthanide-containing minerals are dissolved using acids). Nevertheless, it is very challenging to selectively separate lanthanides from each other since they have very similar physical and chemical properties. Generally, hundreds of cycles of solvent extraction are needed to reach industrially relevant purity, and therefore, the process is highly energyintensive. Additionally, the use of organic solvents contributes to environmental pollution. Accordingly, eco-friendly approaches have been developed, which include the solventfree methods of ion flotation, foam separation, etc.<sup>3–5</sup> These processes use surfactants to attract relevant ions, just as with solvent extraction, but they then remove the ions from the water surface by creating and skimming off foams or by removing precipitates. These methods are less developed for industrial use but are worthy of further study because of their significantly lower environmental impact<sup>5,6</sup> and cost.

While it is clear that the surfactant plays an essential role in all of these extraction processes, what happens at the nanoscale is not fully understood. Because foams and solvent—aqueous emulsions have complex interfaces that are less easily accessed with nanoscale probes, there have been a number of studies of model ion-surfactant systems using floating (Langmuir) monolayers. With monolayers of octadecyl phosphate, a single-chain surfactant, it has been reported that as the lanthanide concentration in the aqueous solution increases, there is a sharp phase-transition-like increase in lanthanide surface density,<sup>8</sup> explained in terms of electrostatic interactions and the presence of ion-ion correlations. Such correlations, as well as the hydration of metal ions,<sup>9</sup> are also found to play a key role in the adsorption of PtCl<sub>6</sub><sup>2-</sup> anionic complexes to floating cationic monolayers through X-ray fluorescence and scattering measurements. 10 At water-oil interfaces, X-ray reflectivity studies 11,12 found surfactant bilayers in the presence of erbium (Er<sup>3+</sup>) ions, and it was proposed that such bilayer formation is an important step in the solvent extraction process. (Lateral ordering was not studied in this system.)

Such bilayer formation increases the number of lanthanide ions at the interface, and this may enhance extraction efficiencies, for either solvent extraction or solvent-free

Received: December 14, 2021 Accepted: January 19, 2022 Published: January 31, 2022





methods. In this study, we investigated the conditions necessary for the formation of lanthanide-containing bilayers at air—water interfaces. Since double-chain phosphates are commonly used in industrial extraction, we used dihexadecyl phosphate (DHDP) floating monolayers as model extractants and explored the effect of type of ions and varying concentrations of ions in the subphase. We find that the formation of bilayers occurs only with heavier lanthanide ions (atomic number  $Z \geq 65$ ) and is correlated with the development of lateral long-range order of the ions.

## EXPERIMENTAL SECTION

**Materials.** Lanthanide chloride salts (LaCl<sub>3</sub>; 99.999%, NdCl<sub>3</sub>; 99.99%, SmCl<sub>3</sub>; 99.99%, GdCl<sub>3</sub>; 99.999%, TbCl<sub>3</sub>; 99.999%, ErCl<sub>3</sub>; 99.995%, and YbCl<sub>3</sub>; 99.998%) were purchased from Sigma-Aldrich and used as received. The salt was dissolved in pure water (18.2 M $\Omega$ cm) to designated concentrations. Dihexadecyl phosphate (DHDP) was also obtained from Sigma-Aldrich and dissolved in chloroform (>99.8%, Fisher Scientific) for a spreading solution.

**Isotherms.** The lanthanide solutions were poured into a Teflon Langmuir trough. A piece of chromatography paper (1 cm width) was used as a Wilhelmy plate to measure the surface pressure. DHDP dissolved in chloroform was spread on the aqueous solution by microsyringe, followed by 20–30 min wait to allow the chloroform to evaporate. The atmosphere above the trough was flushed with helium to reduce X-ray attenuation.

The surface area was controlled by moving the barrier. After spreading the surfactant on the solution, the monolayer was compressed until the desired surface pressure was achieved. The surface pressure and area were recorded during the X-ray measurements. The temperature of the samples was controlled by an integrated water circulation system and set at 20 °C.

**Grazing Incidence X-ray Diffraction (GIXD).** All X-ray experiments were conducted at the 15-ID beamline of the Advanced Photon Source at Argonne National Laboratory. A schematic of the overall X-ray setup is shown in Figure 1. In GIXD, the incident beam

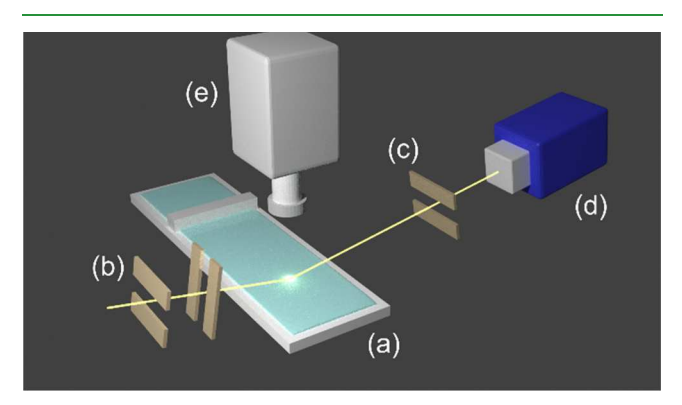


**Figure 1.** Schematic of experiment setup for X-ray study of a Langmuir monolayer. (a) Teflon Langmuir trough with a barrier. (b) Slits to regulate the incident beam size. (c) Horizontal slit for a better resolution along the  $Q_z$ -direction during the X-ray reflectivity measurements. These are replaced with two vertical slits for GIXD measurements for greater resolution in the  $Q_{xy}$ -direction. (d) Pilatus area detector for GIXD and X-ray reflectivity. (e) Vortex detector for fluorescence (XFNTR) measurements.

is incident on the sample at a very small incident angle, below the critical angle for total external reflection. This means that the X-rays will be scattered from the surface region only. We used 10 keV X-rays ( $\lambda=1.239$  Å) and the diffracted photons were collected using a Pilatus area detector. The incident angle is 0.09° above the water surface. The diffraction scans covered the range  $Q_{xy}=0.3-2.6$  Å $^{-1}$ , and the trough was moved by 2 mm horizontally after each scan to

avoid excessive X-ray exposure. We observed no evidence of radiation damage, which would manifest itself as a time dependence of the diffraction pattern.

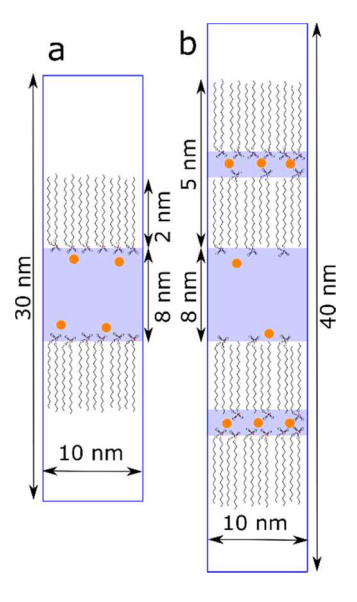
**X-ray Fluorescence Near Total Reflection (XFNTR).** This technique measures the surface concentration of a fluorescing ion. X-rays (10 keV) were incident on the water surface near the critical angle (so that, as before, only the surface region is illuminated with X-rays) and a Vortex detector collected the fluorescence spectrum from the interface. The L $\alpha_{\rm III}$  fluorescence signals were collected for analysis. Further details are given in Bu et al. <sup>13</sup>

**X-ray Reflectivity.** X-ray reflectivity was used to determine the electron density profile normal to the interface, averaged over the x-and y-directions. The intensities of the reflected beam were measured from  $Q_z = 0.016$  to  $0.76 \ \text{Å}^{-1}$ . The sample was moved laterally by 2 mm at regular intervals to avoid radiation damage from the incident beam. The collected reflectivity data were fitted using a slab model. Further details of the fitting methods used and fitting parameters obtained are in the Supporting Information.

All-Atom Explicit Solvent Molecular Dynamics (MD) Simulations. Classical atomistic MD simulations were performed using the package GROMACS (version 2016.3). <sup>14</sup> The CHARMM 36m potential <sup>15</sup> was applied for DHDP, along with the recommended CHARMM TIP3P water model; <sup>16</sup> the structures of which were constrained via the SETTLE algorithm. <sup>17</sup> The CHARMM force field parameters of the Er<sup>3+</sup> ion have been reported in our recent work. <sup>18</sup> These parameters were capable of well reproducing the available experimental data of hydration free energy (–6% deviation from the experimental data), optimal coordination distance between Er<sup>3+</sup> and water oxygen in both the first and the second coordination shells (–3 and 0.4% deviation from the experimental data), and the coordination number in the first coordination shell (0.1% deviation from the experimental data).

Two systems were simulated to examine the molecular structure of the DHDP monolayer and bilayer in the presence of Er<sup>3+</sup> ions (Scheme 1). To simulate the DHDP monolayer system (Scheme 1a), we first generated and equilibrated a regular DHDP bilayer system. In this regular bilayer system (structurally similar to lipid bilayers<sup>19</sup>), 480 DHDP molecules were included, which were surrounded with 26 400 water molecules above and below the bilayer. One hundred sixty Er<sup>3+</sup> ions were included to neutralize the charged DHDP headgroups.

Scheme 1. Schematic Representation of DHDP-Er<sup>3+</sup> Systems Used in Simulations: (a) Monolayer and (b) Bilayer<sup>a</sup>



"Er3" ions are represented by orange beads. Water regions are colored in light blue.

Three-dimensional periodic boundary conditions were employed. The neighbor searching was carried out up to 12 Å using the Verlet particle-based method and was updated every 20 time steps. The Lennard-Jones 12-6 potentials were switched off from 10 to 12 Å using the potential-switch method available in GROMACS. The short-range Coulomb interactions were truncated at 12 Å with the long-range interactions calculated using the Particle mesh Ewald algorithm. 20,21 The NPT ensemble (constant number of particles, pressure, and temperature) was employed. The temperature was coupled using the Nosé-Hover algorithm (reference temperature 298 K, characteristic time 1 ps). The semi-isotropic Parrinello-Rahman barostat was applied with the reference pressure of  $P_{XY} = P_Z = 1$  bar, the characteristic time of 4 ps, and the compressibility of  $4.5 \times 10^{-5}$ bar<sup>-1</sup>. All of the covalent bonds were constrained, which supported an integration time step of 2.5 fs. These parameters were recommended for the accurate reproduction of the original CHARMM simulations on lipid membranes<sup>22</sup> and have been employed in our simulations on proteins<sup>23–26</sup> and lipid membranes.<sup>27</sup> The equilibration run 200 ns, even though the area per DHDP converged to be around 40 Å<sup>2</sup> at around 50 ns. Subsequently, the simulation box length in the Zdimension was enlarged to be 30 nm from around 12.5 nm. The water molecules were shifted in the Z-dimension to the center of the simulation box. The two DHDP layers were now separately attached to the upper and lower surfaces of the water phase at around Z = 19and 11 nm, respectively, forming two DHDP monolayers (Scheme 1a). The vacuum regime with a length of around 18 nm in the Zdimension was included to screen the electrostatic interactions between the simulation box and its images. This DHDP monolayer system was further equilibrated using the NTV ensemble (V stands for volume) for 100 ns. Eventually, the production simulation of 100 ns was conducted using the NTP ensemble, where the semi-isotropic pressure coupling was employed with the zero compressibility in the Z-dimension to retain the vacuum-DHDP monolayer-water-DHDP monolayer-vacuum structure. The temperatures of DHDP, Er3+, and water were separately coupled. The other simulation parameters were the same as those employed in the DHDP regular bilayer system above. The equilibrium area per DHDP was calculated to be  $39.4 \pm 0.1 \text{ Å}^2$ .

In contrast to the DHDP-Er3+ monolayer system, the DHDP-Er3+ (inverted) bilayer system is structurally more complicated (Scheme 1b, see the discussion below). First, a smaller DHDP-Er<sup>3+</sup> (inverted) bilayer structure was generated using packmol.<sup>28</sup> Seven thousand water molecules were distributed in the center region (Z =16-24 nm) of a simulation box (5  $\times$  5  $\times$  40 in  $X \times Y \times Z$ dimensions). Two hundred forty DHDP molecules were distributed at the upper and lower surfaces of the water phase (120 DHDP on each surface). On each surface, half of the DHDP molecules (60) were forming an interdigitated layer at the water surface with the orientations of 30 head-up and 30 head-down; the other 60 DHDP molecules were forming the outmost layer with their alkyl tails pointing toward the vacuum regime. In each of the sandwiched regions between the water-contacting interdigitated layers and vacuum-contacting layers, 30 Er3+ molecules were included to neutralize the charged DHDP headgroups, along with 300 water molecules to account for the hydration behavior of Er<sup>3+</sup> and DHDP headgroups. The bilayer-water-bilayer region was around 18 nm in the Z-dimension (Z = 11-29 nm) surrounded by the vacuum regimes. The system was equilibrated for a duration of 50 ns using the NTP ensemble, where the semi-isotropic pressure coupling was employed with the zero compressibility in the Z-dimension. Subsequently, the system was enlarged by 4 times  $(2 \times 2 \times 1 \text{ in } X)$  $\times$  *Y*  $\times$  *Z* dimensions). After a short equilibration, the long production simulation was conducted for a duration of 150 ns using the same simulation parameters as those in the DHDP-Er3+ monolayer production simulation. The trajectory in the last 50 ns was employed for data collection and analyses, where the equilibrium area per DHDP was calculated to be 19.18  $\pm$  0.04 Å<sup>2</sup>.

#### RESULTS AND DISCUSSION

lon-Specific Effects at Fixed Lanthanide Concentration in the Subphase. The isotherms of DHDP films on solutions with the same ion concentration  $(10^{-4} \text{ M})$  but different lanthanides are shown in Figure 2a. The isotherms of

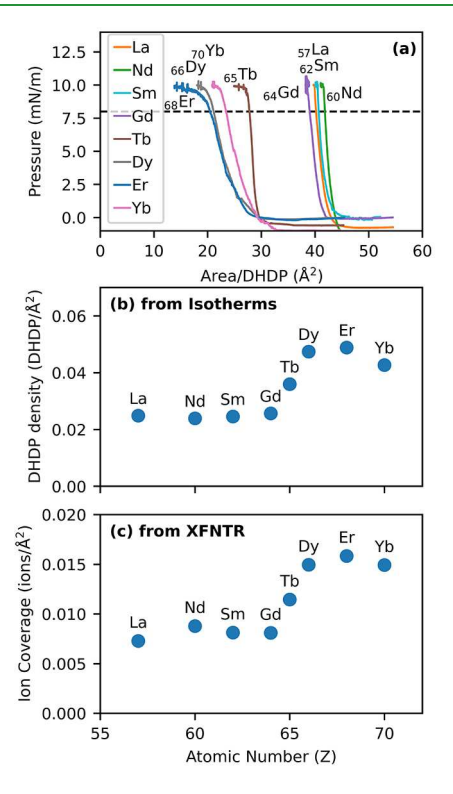


**Figure 2.** (a) Isotherms of DHDP films on various lanthanide solutions. All samples contain  $10^{-4}$  M lanthanide ions in the subphase. The film was compressed until the surface pressure hit 10 mN/m and held at this pressure. (b) Surface density of DHDP obtained from the isotherms (a). The area per molecule values is collected when the surface pressure reaches 8 mN/m (dotted line in (a)) and reversed to get the density (molecule per area). (c) Surface density of the lanthanide ions attracted to the anionic headgroup of DHDP. The ions are attracted from the same bulk ion concentration ( $10^{-4}$  M), and DHDP films are at 10 mN/m during the measurement.

the light elements La<sup>3+</sup> (Z = 57), Nd<sup>3+</sup> (Z = 60), Sm<sup>3+</sup> (Z = 62), and Gd<sup>3+</sup> (Z = 64) are similar to each other. They share about the same molecular area ( $\sim$ 40 Å<sup>2</sup>/molecule) when compressed, roughly what is expected for a closely packed monolayer of double-chain molecules at the air—water interface.<sup>29</sup>

The isotherms of heavier lanthanides are quite different. The limiting molecular areas when compressed are approximately halved (~20 Ų/molecule), consistent with bilayer formation. Tb³+ (Z=65) has an isotherm that falls between the light and heavy cases.

Figure 2b shows the density of the DHDP molecules at the interface, calculated from the isotherms in Figure 2a at a pressure of 8 mN/m. In the presence of lighter lanthanides, there are  $\sim 0.025$  DHDP molecules per Å<sup>2</sup>. With heavier lanthanides, the DHDP densities are doubled ( $\sim 0.05$  DHDP/ Å<sup>2</sup>). Tb<sup>3+</sup> is again an intermediate case.

To measure the surface density of lanthanide ions directly, we used X-ray fluorescence near total reflection (XFNTR), with the monolayer held at pressures of 10 mN/m. The

observed surface densities (ions/Å<sup>2</sup>) of lanthanide ions are shown in Figure 2c. For lighter lanthanides, up to  $Gd^{3+}$  (Z =64), there are about 0.008 ions/Å<sup>2</sup>. Heavier lanthanides, from  $\mathrm{Dy}^{3+}$  (Z = 66) to Yb<sup>3+</sup> (Z = 70), have roughly twice the areal density (0.015 ions/Å<sup>2</sup>). Tb<sup>3+</sup> again falls into an intermediate region, with 0.011 Tb<sup>3+</sup>/ $Å^2$  at the surface.

For all lanthanides, the DHDP density (Figure 2b) is roughly 3 times the ion density determined from XFNTR (Figure 2c). This is consistent with the charge balance between single-charged DHDP triply charged lanthanides, without contributions from H+ or OH- ions. Neither XFNTR nor isotherms tell us the orientation of the molecules in the bilayer. Two earlier studies have found (using X-ray reflectivity) that an inverted bilayer of DHDP forms at an oil-water interface in the presence of erbium ions. 11,12 In the inverted bilayers, the polar headgroups of DHDP (along with the associated Ln(III) ions) are embedded inside the bilayer, while nonpolar alkyl tails are pointing toward either the oil phase or the water phase, even though the last orientation is energetically unfavorable owing to the hydrophobic feature of the tails. We performed X-ray reflectivity scans for the floating DHDP monolayer on 10<sup>-4</sup> M Nd<sup>3+</sup>, Gd<sup>3+</sup>, Tb<sup>3+</sup>, and Er<sup>3+</sup> solutions. These scans are shown in Figure 3a, and the fitted electron density profiles (EDPs) are shown in Figure 3b.

With Nd<sup>3+</sup> and Gd<sup>3+</sup>, a DHDP monolayer structure (waterheadgroup-tail-air) is confirmed by reflectivity data. The electron density of the tail layer of both samples is 0.30 electrons/Å<sup>3</sup>. This means that DHDPs are forming a closely packed monolayer structure over Nd3+ and Gd3+ solutions, as expected from the XFNTR and isotherm data shown above.

With Tb<sup>3+</sup> or Er<sup>3+</sup> in the subphase, a DHDP interdigitated inverted bilayer structure is observed. Unlike the case of the oil-water interface, 11,12 our measurements can only be fitted by introducing a small electron-dense slab between the water and bottom tail region (water-head-tail-head-tail-air). The presence of the bottom head layer indicates that there are some DHDPs in the bottom half facing downward (headgroup next to the water). Zhang et al. studied a spontaneous collapse, which eventually caused monolayer molecules (palmitic acid, with calcium ions in the subphase) to form an inverted bilayer.<sup>30</sup> According to their molecular dynamics simulation, the bilayer formation process is nucleated by corrugation of the surface and ejection of the monolayer. Subsequently, the inverted bilayer grows by transporting molecules from the monolayer region. In their video of the simulation, some of the molecules transported to the inverted bilayer region are oriented in the "wrong" direction, just as our reflectivity data show. Although we do not observe the dynamics of bilayer formation, it is possible that in our system the same process of corrugation and folding leads to the inverted bilayer structure.

Ion-Specific Effects in the Lanthanide Concentration Dependence. For Er<sup>3+</sup> and Nd<sup>3+</sup>, the surface densities of erbium ions under floating DHDP monolayers were measured by XFNTR in the subphase concentration range of  $10^{-8}$ – $10^{-3}$ M. Figure 4a shows the surface densities of DHDP molecules as a function of the subphase lanthanide concentration, at 8 mN/m, derived from isotherms (not shown).

Figure 4b shows the surface densities of Er3+ or Nd3+ ions, also as a function of the subphase concentration. There are two rather sharp transitions in XFNTR data. Er3+ and Nd3+ both undergo the first transition around  $(2-3) \times 10^{-7}$  M, but only Er<sup>3+</sup> undergoes the second transition. The first step is the onset of surface adsorption of the lanthanide ion, and it is similar to

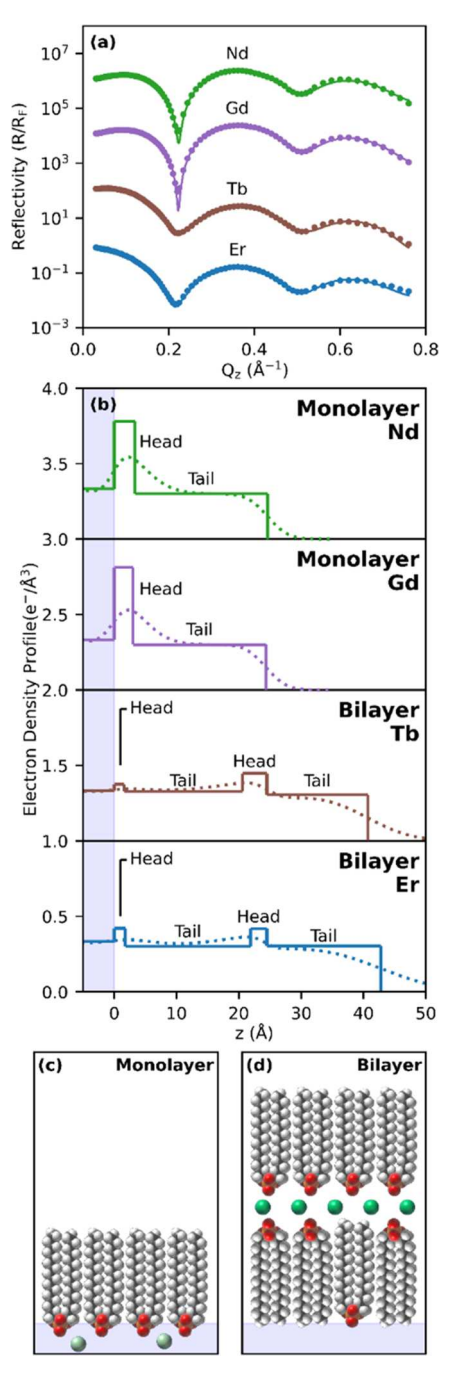


Figure 3. (a) X-ray reflectivity data for DHDP floating monolayers at 10 mN/m with  $10^{-4} \text{ M}$  lanthanide ions in the subphase (green:  $Nd^{3+}$ , purple: Gd<sup>3+</sup>, brown: Tb<sup>3+</sup>, and blue: Er<sup>3+</sup>). Solid lines represent the best fits using slab models. The data sets and fits are shifted vertically for clarity. (b) Electron density profiles determined from model fits. The blue region (Z < 0) is water and the surface is at Z = 0. The solid lines show the slabs without interface roughness. Cartoon representations of (c) the DHDP monolayer structure formed with light lanthanide ions and (d) the bilayer structure formed with heavy lanthanide ions.

that previously reported with a single-chain surfactant monolayer. Past the first step, there are about 0.008 ions/Å<sup>2</sup> at the interface for both Er3+ and Nd3+. However, there is another jump of the number density of surface Er3+ ions at a subphase concentration of about 10<sup>-5</sup> M. This second transition roughly doubles the number of erbium ions attracted

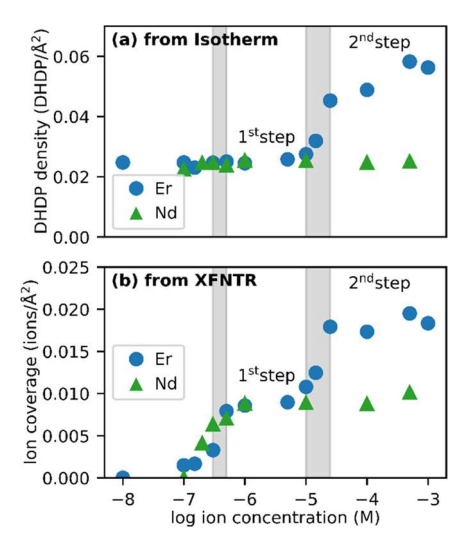


Figure 4. (a) DHDP surface density as a function of bulk ion concentration in the subphase. The density values were calculated from the isotherms at  $\sim 8$  mN/m. The ranges of the first and second transitions are indicated as light gray regions. (b) Ion surface densities from the same samples, measured by XFNTR, as functions of subphase ion concentration.

to the surface. The transition from the first to the second step occurs because the DHDP monolayer collapses to an inverted bilayer structure, as described earlier.

The twofold transitions of the Er3+ XFNTR result can be explained by comparison to the DHDP surface density (Figure 4a). With dilute  $Er^{3+}$  and  $Nd^{3+}$  subphases (<10<sup>-5</sup> M  $Er^{3+}$ ), the DHDP monolayer has a limiting area of 0.025 DHDP/Å<sup>2</sup>, which corresponds to 40 Å<sup>2</sup>/molecule, as expected for a twochain molecule. The measured area per DHDP is also similar to the previously calculated value of  $\sim$ 43 Å<sup>2</sup>/lipid in the twotail DLPS lipid bilayer system in the presence of La(III) ions, where the gel phase of DLPS molecules was reached. 19 There is no significant change in the area/molecule across the first transition because they form a monolayer both before and after the first transition. Above the second transition, at subphase Er<sup>3+</sup> concentration of 10<sup>-5</sup> M, there is an approximate doubling of the number of DHDP molecules per unit area just where there is a second transition (with Er3+ only) in Figure 4b. Thus, both isotherm and XFNTR data are consistent with the formation of a bilayer when the Er3+ concentration in the subphase is above 10<sup>-5</sup> M. With Nd<sup>3+</sup>, on the other hand, there is a constant DHDP density for the whole range of subphase concentrations, meaning that there is always only a monolayer. At all subphase concentrations, there is roughly a 3:1 ratio of DHDP density to ion density.

X-ray reflectivity confirms these conclusions. There is a monolayer below the second transition in  $\mathrm{Er^{3^+}}$ , but a bilayer above it (Figure 5). Incidentally, at the oil—water interface,  $^{11,12}$  the bilayer structure was reported at a much lower lanthanide concentration,  $5 \times 10^{-7}$  M  $\mathrm{ErBr_3}$ . (Only a single concentration was used in that study.) Since the oil phase is more oleophilic than air, it is reasonable that a bilayer would be formed more easily in that system.

The lateral ordering of ions under DHDP floating monolayers was reported by Miller et al.<sup>31</sup> With a subphase containing  $10^{-4}$  M ErCl<sub>3</sub>, the ion lattice is hexagonal, resulting in a single peak at  $Q_{xy} = 0.512 \text{ Å}^{-1}$  (Figure 6). However, both ionic and DHDP structures are shifted as the subphase

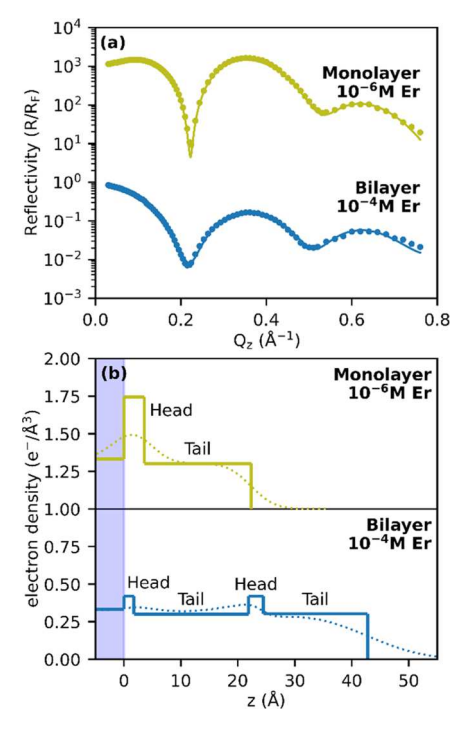


**Figure 5.** (a) Reflectivity data for DHDP over a subphase with  $ErCl_3$  concentrations above and below the second transition. The best fits are shown by solid lines. The reflectivity data and fits are shifted vertically for clarity. (b) Electron density profiles (dotted lines) and slabs without interface roughness (solid lines) for the best fits. The light blue region indicates water; the surface of water is at z=0.

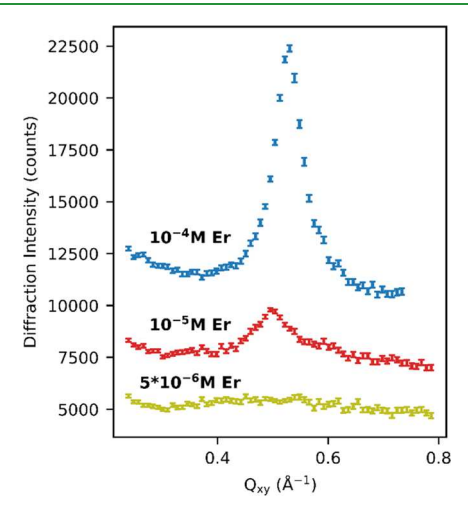


**Figure 6.** GIXD scans for three subphase concentrations, as labeled. The intensity is integrated along the  $Q_z$ -direction (0–0.7 Å<sup>-1</sup>). There is lateral order of Er ions only when a bilayer is formed (at and above  $10^{-5}$  M). Peaks due to the molecular monolayer are in a higher  $Q_{xy}$  range and are not shown. The scans are shifted vertically for clarity.

concentration decreases. No ionic peak is observed from  $5 \times 10^{-6}$  M sample, which clarifies the fact that there is no ion—ion correlation with the monolayer structure. The ionic peak is observed from  $10^{-4}$  and  $10^{-5}$  M samples at slightly different  $Q_{xy}$ . The  $10^{-4}$  M sample has a peak at  $Q_{xy} = 0.529$  Å<sup>-1</sup>, and the intermediate sample  $(10^{-5}$  M) has the same peak at  $Q_{xy} = 0.502$  Å<sup>-1</sup>. This result indicates that when the sample is on the second step, the ions form a shorter lattice vector  $(d = 2\pi/Q_{xy})$  than that from the intermediate state. Consequently, the ions

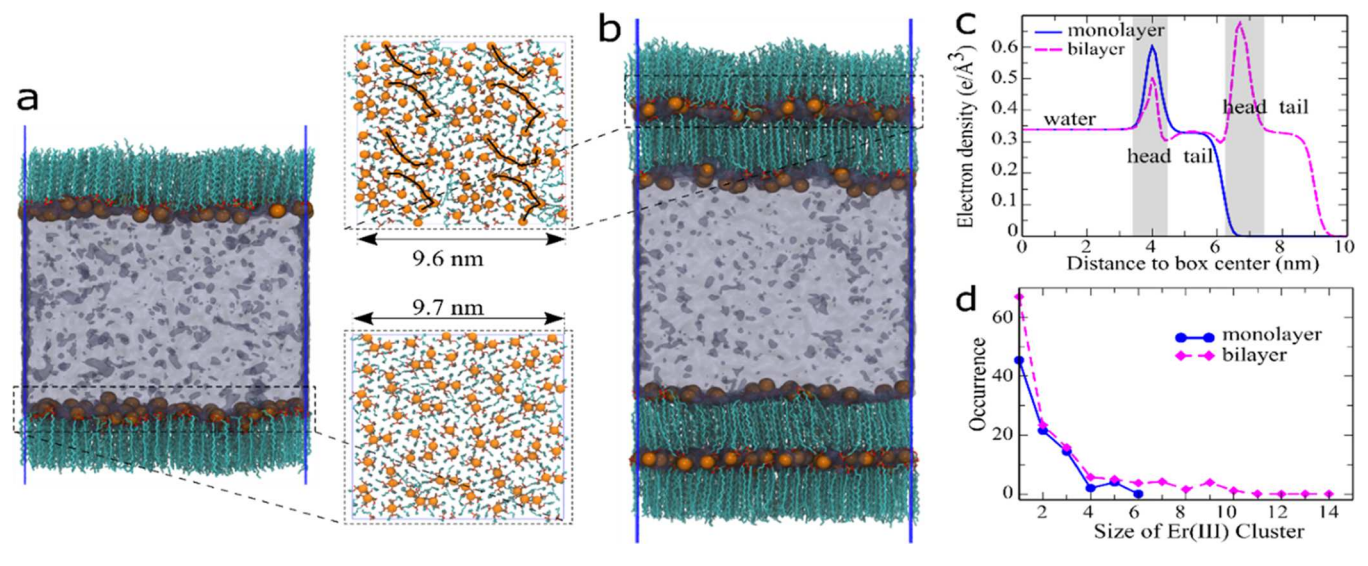


Figure 7. Atomistic simulation snapshots of the equilibrated structure of the (a) monolayer and (b) bilayer for DHDP-Er3+ systems. Er ions are colored in orange, and water is transparent and colored light blue. Insets are the top views of Er3+ ions in the highlighted regions. In the bilayer system, the sandwiched Er3+ ions are forming linear aggregates, highlighted via black curves. The blue lines represent the simulation box. (c) Electron density of all molecules (water, DHDP, Er<sup>3+</sup>) as a function of the distance to the center of the simulation box. The DHDP head and tail regions are highlighted, as well as the water subphase. (d) Histogram plot of the distribution of Er(III) cluster sizes. The lines are guides to the eye.

in the 10<sup>-4</sup> M sample have a stronger ion—ion correlation than in the  $10^{-5}$  M sample due to the shorter interaction distance.

All-Atom Explicit Solvent MD Simulations. To explore molecular structures, we conducted two atomistic simulations. The DHDP-Er<sup>3+</sup> monolayer system (Figure 7a) is employed to stand for the experimental system with the subphase Er3+ concentration range of  $3 \times 10^{-6} - 10^{-5}$  M, where a DHDP monolayer was observed. The DHDP-Er3+ bilayer simulation (Figure 7b) was performed to represent the experimental system with the subphase Er<sup>3+</sup> concentration above 10<sup>-5</sup> M, where a bilayer structure best fits the reflectivity data (Figure

In the monolayer system, the area per DHDP in the simulation was  $39.4 \pm 0.1 \text{ Å}^2/\text{DHDP}$ , in good agreement with the experimental value of the 40 Å<sup>2</sup>/DHDP. The area per DHDP dropped to 19.18  $\pm$  0.04 Å<sup>2</sup>/DHDP in the bilayer system. We also calculated electron density profiles (Figure 7c). The average electron density in the water subphase (0.338 e/Å<sup>3</sup>) and in DHDP alkyl tail regions (approximately 0.33 e/ Å<sup>3</sup>) are in line with the corresponding experimental data (Figure 5b). The peak electron densities in the DHDP head regions are qualitatively consistent with the experimental results in Figure 5b. The quantitative differences likely originate in the differences in the structures: in atomistic simulations, the numerical ratio of head-up DHDP to headdown DHDP in water-contacting layers is 1:1 (Scheme 1) and the ratio of water to Er<sup>3+</sup> ions is 10:1 in the sandwiched region between the water-contacting layer and the air-contacting layer; these quantities are experimentally unknown. Nevertheless, in general, our simulations are representative of the experimental systems.

The insets in Figure 7 provide visual support that Er<sup>3+</sup> ions are highly dispersed in the monolayer system (Figure 7a), whereas they are linearly aggregated in the sandwiched region in the bilayer system (Figure 7b). Cluster calculations (Figure 7d) indicate that in the bilayer system Er<sup>3+</sup> clusters as large as 14 mer exist, which are much larger than those in the monolayer system, where up to 6 mer of Er<sup>3+</sup> clusters formed.

We further calculated the coordination behavior of Er<sup>3+</sup> in the two systems (Table 1). The optimal coordination distance

Table 1. Coordination of Er3+ Ions from All-Atom Simulations

	$Er-O(H_2O)$		Er-O(DHDP)	
	$r (Å)^a$	CN <sup>b</sup>	$r (Å)^a$	CN <sup>b</sup>
monolayer	2.30	4.6	2.16	3.4
bilayer (water-DHDP interface)	2.30	5.0	2.16	3.0
bilayer (sandwiched region <sup>c</sup> )	2.30	4.1	2.16	3.9

<sup>a</sup>Optimal Er-O distance obtained from the peak position of the corresponding radial distribution function. <sup>b</sup>Coordination number (CN) in the first coordination shell. "Sandwiched region" refers to the regions between the vacuum-contacting DHDP monolayer and the water-contacting interdigitated DHDP layer.

of  ${\rm Er^{3+}}$  to water oxygen is 2.3 Å, in good agreement with X-ray experimental data <sup>32,33</sup> and our recent computational work. <sup>18</sup> In contrast, the coordination distance of Er<sup>3+</sup> to DHDP oxygen is slightly shifted to a shorter value of 2.16 Å, which is ascribed to strong electrostatic interactions between Er3+ ions and oppositely charged DHDP headgroups. This is in line with our recent finding that enhanced interactions of metal ions and ligands will decrease their equilibrium coordination distance, although lower valent metal ions (NpO2+ and NpO2+) were employed there.<sup>34</sup> Meanwhile, the total coordination number remains a constant of 8 in both systems, in good agreement with X-ray data<sup>32,33</sup> and computational results<sup>18</sup> in bulk water solutions, suggesting the independence of the coordination of Er<sup>3+</sup> on the local environment (solution vs interface). Surprisingly, Table 1 also shows that the Er-DHDP coordination is elevated in the sandwiched region than that at the water-DHDP interface, evidenced by the increased coordination of negatively charged DHDP around Er3+ ions. This originates in the fact that the dehydration in the sandwiched regions lowers the local relative permittivity, consequently enhancing the coulomb attractive interactions

between Er<sup>3+</sup> and DHDP. Figure 8 presents the typical Er<sup>3+</sup> coordination structure at the water–DHDP interface and in

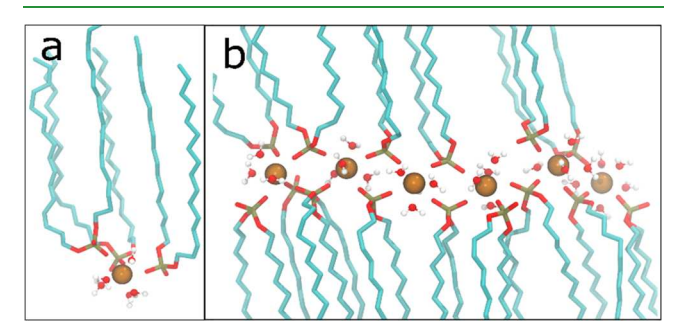


**Figure 8.** Local coordination structure of Er<sup>3+</sup> ions (orange beads) at (a) the water–DHDP interface and (b) the sandwiched region between the water-contacting DHDP layer and the vacuum-contacting layer. Water O/H are colored in red/white, respectively; DHDP O/P/C atoms in red/tan/cyan, respectively. DHDP hydrogen and other noncoordinating molecules are omitted for display.

the sandwiched regions. It also demonstrates that the neighboring  $\mathrm{Er^{3+}}$  ions in the sandwiched region are bridged by the DHDP headgroups, forming  $\mathrm{Er^{3+}}$  aggregates in the inset of Figure 7b.

#### CONCLUSIONS

At first glance, all trivalent lanthanides should be chemically identical. Of course, it is well known that they are not identical in practice, but this study reveals new and unexpected differences in interfacial behavior. Many of the previously known differences were attributed to the sizes of ions and the numbers of water molecules in their hydration shells. It is possible that the same differences explain our observations also, but this is not established.

We have found that the interactions of ions with surfactant interfaces take place in phase-transition-like steps as a function of the ion concentration in the aqueous subphase. In addition to the previously reported first step, below which there are no adsorbed ions, we find that there is a second step at higher concentrations leading to a bilayer, but only for heavier lanthanides. In these bilayers, lanthanide ions are laterally ordered. This is reminiscent of what has been observed in a different case, that of charge inversion in colloids. It was predicted, 35–38 and experimentally observed, 39,40 that when there is an excess of counterions at an interface, this is made energetically favorable by the lateral ordering of counterions. We see the same lateral ordering in this case when the number of ions at the interface doubles due to bilayer formation.

Although the formation of an inverted bilayer at an oil—water interface has been reported previously, the air—water interface allows a more detailed study of the conditions leading to the formation of such bilayers. Since the bilayer selectively isolates heavier lanthanides, we suggest that one can enhance the efficiency of extraction processes by reproducing the conditions leading to bilayer formation. Quite generally, these studies reveal further ways in which lanthanides show unexpected ion-specific behaviors.

#### ASSOCIATED CONTENT

## Supporting Information

The Supporting Information is available free of charge at https://pubs.acs.org/doi/10.1021/acsami.1c24008.

X-ray reflectivity fitting details and best-fit parameters (PDF)

## AUTHOR INFORMATION

## **Corresponding Author**

Pulak Dutta — Department of Physics & Astronomy, Northwestern University, Evanston, Illinois 60208, United States; orcid.org/0000-0002-2111-0546; Email: pdutta@northwestern.edu

#### **Authors**

Sangjun Yoo — Department of Physics & Astronomy, Northwestern University, Evanston, Illinois 60208, United States; © orcid.org/0000-0003-0525-204X

Baofu Qiao – Department of Materials Science and Engineering, Northwestern University, Evanston, Illinois 60208, United States

Travis Douglas — Department of Physics & Astronomy, Northwestern University, Evanston, Illinois 60208, United States; © orcid.org/0000-0002-0817-7674

Wei Bu — Center for Advanced Radiation Sources, University of Chicago, Chicago, Illinois 60637, United States;
orcid.org/0000-0002-9996-3733

Monica Olvera de la Cruz – Department of Physics & Astronomy, Northwestern University, Evanston, Illinois 60208, United States; Department of Materials Science and Engineering, Northwestern University, Evanston, Illinois 60208, United States

Complete contact information is available at: https://pubs.acs.org/10.1021/acsami.1c24008

## Notes

The authors declare no competing financial interest.

## ■ ACKNOWLEDGMENTS

This research was supported by the National Science Foundation under grant number DMR-2004557. B.Q. and M.O.d.l.C. were supported by the grant DE-FG02-08ER46539 funded by the U.S. Department of Energy, Office of Science. ChemMatCARS Sector 15 is supported by the National Science Foundation under grant number NSF/CHE-1834750. This research used resources of the Advanced Photon Source, a U.S. Department of Energy (DOE) Office of Science User Facility operated for the DOE Office of Science by Argonne National Laboratory under Contract No. DE-AC02-06CH11357.

#### REFERENCES

- (1) Xie, F.; Zhang, T. A.; Dreisinger, D.; Doyle, F. A critical review on solvent extraction of rare earths from aqueous solutions. *Miner. Eng.* **2014**, *56*, 10–28.
- (2) Hidayah, N. N.; Abidin, S. Z. The evolution of mineral processing in extraction of rare earth elements using liquid-liquid extraction: A review. *Miner. Eng.* **2018**, *121*, 146–157.
- (3) Nicol, S. K.; Galvin, K. P.; Engel, M. D. Ion flotation potential applications to mineral processing. *Miner. Eng.* **1992**, *5*, 1259–1275.
- (4) Doyle, F. M. Ion flotation—its potential for hydrometallurgical operations. *Int. J. Miner. Process.* **2003**, *72*, 387–399.
- (5) Chang, L.; Cao, Y.; Fan, G.; Li, C.; Peng, W. A review of the applications of ion floatation: Wastewater treatment, mineral beneficiation and hydrometallurgy. *RSC Adv.* **2019**, *9*, 20226–20239.
- (6) Shetty, S.; Chernyshova, I. V.; Ponnurangam, S. Foam flotation of rare earth elements by conventional and green surfactants. *Miner. Eng.* **2020**, *158*, No. 106585.

- (7) Sholl, D. S.; Lively, R. P. Seven chemical separations to change the world. *Nature* **2016**, *532*, 435–437.
- (8) Miller, M.; Liang, Y.; Li, H.; Chu, M.; Yoo, S.; Bu, W.; Olvera de la Cruz, M.; Dutta, P. Electrostatic Origin of Element Selectivity during Rare Earth Adsorption. *Phys. Rev. Lett.* **2019**, *122*, No. 058001.
- (9) Nayak, S.; Kumal, R. R.; Liu, Z.; Qiao, B.; Clark, A. E.; Uysal, A. Origins of Clustering of Metalate–Extractant Complexes in Liquid–Liquid Extraction. *ACS Appl. Mater. Interfaces* **2021**, *13*, 24194–24206.
- (10) Uysal, A.; Rock, W.; Qiao, B.; Bu, W.; Lin, B. Two-Step Adsorption of PtCl62— Complexes at a Charged Langmuir Monolayer: Role of Hydration and Ion Correlations. *J. Phys. Chem.* C 2017, 121, 25377—25383.
- (11) Liang, Z.; Bu, W.; Schweighofer, K. J.; Walwark, D. J.; Harvey, J. S.; Hanlon, G. R.; Amoanu, D.; Erol, C.; Benjamin, I.; Schlossman, M. L. Nanoscale view of assisted ion transport across the liquid—liquid interface. *Proc. Natl. Acad. Sci. U.S.A.* **2019**, *116*, 18227.
- (12) Bu, W.; Yu, H.; Luo, G.; Bera, M. K.; Hou, B.; Schuman, A. W.; Lin, B.; Meron, M.; Kuzmenko, I.; Antonio, M. R.; Soderholm, L.; Schlossman, M. L. Observation of a Rare Earth Ion–Extractant Complex Arrested at the Oil–Water Interface During Solvent Extraction. *J. Phys. Chem. B* **2014**, *118*, 10662–10674.
- (13) Bu, W.; Mihaylov, M.; Amoanu, D.; Lin, B.; Meron, M.; Kuzmenko, I.; Soderholm, L.; Schlossman, M. L. X-ray Studies of Interfacial Strontium—Extractant Complexes in a Model Solvent Extraction System. *J. Phys. Chem. B* **2014**, *118*, 12486–12500.
- (14) Hess, B.; Kutzner, C.; van der Spoel, D.; Lindahl, E. GROMACS 4: Algorithms for Highly Efficient, Load Balanced, and Scalable Molecular Simulation. *J. Chem. Theory Comput.* **2008**, *4*, 435–447.
- (15) Huang, J.; Rauscher, S.; Nawrocki, G.; Ran, T.; Feig, M.; de Groot, B. L.; Grubmuller, H.; MacKerell, A. D., Jr. CHARMM36m: An Improved Force Field for Folded and Intrinsically Disordered Proteins. *Nat. Methods* **2017**, *14*, 71–73.
- (16) MacKerell, A. D.; Bashford, D.; Bellott, M.; Dunbrack, R. L.; Evanseck, J. D.; Field, M. J.; Fischer, S.; Gao, J.; Guo, H.; Ha, S.; Joseph-McCarthy, D.; Kuchnir, L.; Kuczera, K.; Lau, F. T. K.; Mattos, C.; Michnick, S.; Ngo, T.; Nguyen, D. T.; Prodhom, B.; Reiher, W. E.; Roux, B.; Schlenkrich, M.; Smith, J. C.; Stote, R.; Straub, J.; Watanabe, M.; Wiorkiewicz-Kuczera, J.; Yin, D.; Karplus, M. All-Atom Empirical Potential for Molecular Modeling and Dynamics Studies of Proteins. *J. Phys. Chem. B* 1998, 102, 3586–3616.
- (17) Miyamoto, S.; Kollman, P. A. SETTLE: An Analytical Version of the SHAKE and RATTLE Algorithm for Rigid Water Models. *J. Comput. Chem.* **1992**, *13*, 952–962.
- (18) Qiao, B.; Skanthakumar, S.; Soderholm, L. Comparative CHARMM and AMOEBA Simulations of Lanthanide Hydration Energetics and Experimental Aqueous Solution Structures. *J. Chem. Theory Comput.* **2018**, *14*, 1781–1790.
- (19) Qiao, B.; Olvera de la Cruz, M. Driving Force for Crystallization of Anionic Lipid Membranes Revealed by Atomistic Simulations. *J. Phys. Chem. B* **2013**, *117*, 5073–5080.
- (20) Darden, T.; York, D.; Pedersen, L. Particle Mesh Ewald: An N-log(N) Method for Ewald Sums in Large Systems. *J. Chem. Phys.* **1993**, *98*, 10089–10092.
- (21) Essmann, U.; Perera, L.; Berkowitz, M. L.; Darden, T.; Lee, H.; Pedersen, L. A Smooth Particle Mesh Ewald Method. *J. Chem. Phys.* **1995**, *103*, 8577–8593.
- (22) Lee, J.; Cheng, X.; Swails, J. M.; Yeom, M. S.; Eastman, P. K.; Lemkul, J. A.; Wei, S.; Buckner, J.; Jeong, J. C.; Qi, Y.; Jo, S.; Pande, V. S.; Case, D. A.; Brooks, C. L.; MacKerell, A. D.; Klauda, J. B.; Im, W. CHARMM-GUI Input Generator for NAMD, GROMACS, AMBER, OpenMM, and CHARMM/OpenMM Simulations Using the CHARMM36 Additive Force Field. *J. Chem. Theory Comput.* 2016, 12, 405–413.
- (23) Panganiban, B.; Qiao, B.; Jiang, T.; DelRe, C.; Obadia, M. M.; Nguyen, T. D.; Smith, A. A. A.; Hall, A.; Sit, I.; Crosby, M. G.; Dennis, P. B.; Drockenmuller, E.; Olvera de la Cruz, M.; Xu, T.

- Random Heteropolymers Preserve Protein Function in Foreign Environments. *Science* **2018**, *359*, 1239–1243.
- (24) Qiao, B.; Lopez, L.; Olvera de la Cruz, M. "Mirror"-Like Protein Dimers Stabilized by Local Heterogeneity at Protein Surfaces. *J. Phys. Chem. B* **2019**, *123*, 3907–3915.
- (25) Qiao, B.; Jiménez-Ángeles, F.; Nguyen, T. D.; Olvera de la Cruz, M. Water Follows Polar and Nonpolar Protein Surface Domains. *Proc. Natl. Acad. Sci. U.S.A.* **2019**, *116*, 19274–19281.
- (26) Qiao, B.; Olvera de la Cruz, M. Enhanced Binding of SARS-CoV-2 Spike Protein to Receptor by Distal Polybasic Cleavage Sites. *ACS Nano* **2020**, *14*, 10616–10623.
- (27) Jiang, T.; Hall, A.; Eres, M.; Hemmatian, Z.; Qiao, B.; Zhou, Y.; Ruan, Z.; Couse, A. D.; Heller, W. T.; Huang, H.; de la Cruz, M. O.; Rolandi, M.; Xu, T. Single-chain heteropolymers transport protons selectively and rapidly. *Nature* **2020**, *577*, 216–220.
- (28) Martínez, L.; Andrade, R.; Birgin, E. G.; Martínez, J. M. PACKMOL: A Package for Building Initial Configurations for Molecular Dynamics Simulations. *J. Comput. Chem.* **2009**, *30*, 2157–2164.
- (29) Kaganer, V. M.; Möhwald, H.; Dutta, P. Structure and phase transitions in Langmuir monolayers. *Rev. Mod. Phys.* **1999**, *71*, 779–819
- (30) Zhang, P.; Pham, T.; Zheng, X.; Liu, C.; Plata, P. L.; Král, P.; Bu, W.; Lin, B.; Liu, Y. Spontaneous collapse of palmitic acid films on an alkaline buffer containing calcium ions. *Colloids Surf., B* **2020**, *193*, No. 111100.
- (31) Miller, M.; Chu, M.; Lin, B.; Bu, W.; Dutta, P. Atomic Number Dependent "Structural Transitions" in Ordered Lanthanide Monolayers: Role of the Hydration Shell. *Langmuir* **2017**, 33, 1412–1418.
- (32) Habenschuss, A.; Spedding, F. H. The Coordination (Hydration) of Rare Earth ions in Aqueous Chloride Solutions from X-Ray Diffraction. I.TbCl<sub>3</sub>,DyCl<sub>3</sub>, ErCl<sub>3</sub>,TmCl<sub>3</sub>,and LuCl<sub>3</sub>. *J. Chem. Phys.* **1979**, *70*, 2797–2806.
- (33) Habenschuss, A.; Spedding, F. H. The Coordination (Hydration) of Rare Earth ions in Aqueous Chloride Solutions from X-Ray Diffraction. II. LaCl<sub>3</sub>, PrCl<sub>3</sub>, and NdCl<sub>3</sub>. *J. Chem. Phys.* **1979**, 70, 3758–3763.
- (34) Estes, S. L.; Qiao, B.; Jin, G. B. Ion Association with Tetra-nalkylammonium Cations Stabilizes Higher-oxidation-state Neptunium Dioxocations. *Nat. Commun.* **2019**, *10*, No. 59.
- (35) Labbez, C.; Jönsson, B.; Skarba, M.; Borkovec, M. Ion–Ion Correlation and Charge Reversal at Titrating Solid Interfaces. *Langmuir* **2009**, *25*, 7209–7213.
- (36) Kondrat, S.; Georgi, N.; Fedorov, M. V.; Kornyshev, A. A. A superionic state in nano-porous double-layer capacitors: insights from Monte Carlo simulations. *Phys. Chem. Chem. Phys.* **2011**, *13*, 11359–11366
- (37) Wernersson, E.; Kjellander, R.; Lyklema, J. Charge Inversion and Ion—Ion Correlation Effects at the Mercury/Aqueous MgSO4 Interface: Toward the Solution of a Long-Standing Issue. *J. Phys. Chem. C* **2010**, *114*, 1849—1866.
- (38) Mendez-Morales, T.; Burbano, M.; Haefele, M.; Rotenberg, B.; Salanne, M. Ion-ion correlations across and between electrified graphene layers. *J. Chem. Phys.* **2018**, *148*, No. 193812.
- (39) Tan, Q.; Zhao, G.; Qiu, Y.; Kan, Y.; Ni, Z.; Chen, Y. Experimental Observation of the Ion—Ion Correlation Effects on Charge Inversion and Strong Adhesion between Mica Surfaces in Aqueous Electrolyte Solutions. *Langmuir* **2014**, *30*, 10845–10854.
- (40) Futamura, R.; Iiyama, T.; Takasaki, Y.; Gogotsi, Y.; Biggs, M. J.; Salanne, M.; Ségalini, J.; Simon, P.; Kaneko, K. Partial breaking of the Coulombic ordering of ionic liquids confined in carbon nanopores. *Nat. Mater.* **2017**, *16*, 1225–1232.
- (41) Nayak, S.; Kumal, R. R.; Uysal, A. Chemrxiv 2021, DOI: 10.33774/chemrxiv-2021-pzxn9-v2.

## ■ NOTE ADDED IN PROOF

We have been informed of an unpublished recent study by Nayak, Kumal and Uysal<sup>41</sup> that is consistent with what we

report in this paper. They observed inverted bilayer formation at the air-water interface in the presence of Lu3+ (the heaviest lanthanide).

